






Structures in the terms of the Vlasov equation observed at Earth's magnetopause

J. R. Shuster^{1,2}  , D. J. Gershman², J. C. Dorelli², B. L. Giles², S. Wang^{1,2}, N. Bessho^{1,2}, L.-J. Chen², P. A. Cassak³, S. J. Schwartz^{4,5}, R. E. Denton⁶, V. M. Uritsky^{2,7}, W. R. Paterson², C. Schiff², A. F. Viñas^{2,7}, J. Ng^{1,2}, L. A. Avanov^{1,2}, D. E. da Silva^{2,8} and R. B. Torbert ^{9,10}

The Vlasov equation describes collisionless plasmas in the continuum limit and applies to many fundamental plasma energization phenomena. Because this equation governs the evolution of plasma in six-dimensional phase space, studies of its structure have mostly been limited to numerical or analytical methods. Here terms of the Vlasov equation are determined from observations of electron phase-space density gradients measured by the four Magnetospheric Multiscale spacecraft in the vicinity of magnetic reconnection at Earth's magnetopause. We identify which electrons in velocity space substantially support the electron pressure divergence within electron-scale current layers. Furthermore, we isolate and characterize the effects of density, velocity and temperature gradients on the velocity-space structure and dynamics of these electrons. Unipolar, bipolar and ring structures in the electron phase-space density gradients are compared to a simplified Maxwellian model and correspond to localized gradients in density, velocity and temperature, respectively. These structures have implications for the ability of collisionless plasmas to maintain kinetic Vlasov equilibrium. The results provide a kinetic perspective relevant to how the electron pressure divergence may develop to violate the electron frozen-in condition and sustain electron-scale energy conversion processes, such as the reconnection electric field, in collisionless space plasma environments.

An exact description for collisionless plasmas in the continuum limit is provided by the Vlasov equation^{1,2}. This kinetic description of plasmas is required to understand many fundamental plasma energization phenomena^{3–10}, especially the explosive energy conversion process of magnetic reconnection known to operate ubiquitously within plasmas throughout the Universe^{11–17}. The literature contains an extensive amount of analytical advances concerning the long-standing problem of finding general equilibrium solutions to the Vlasov–Maxwell system^{18,19}. Harris²⁰ presented an exact solution to the Vlasov equation that is widely utilized to initialize kinetic simulations of symmetric magnetic reconnection^{21–25}. Despite the idealizations employed, remarkably, the Harris sheet model agrees well with observations taken from laboratory reconnection experiments²⁶. More complexity is required for the asymmetric current sheet configuration, where plasma parameters such as the density, temperature and magnetic field strength vary across the layer, which is typical of the reconnection environment at Earth's dayside magnetopause. Although not an exact kinetic equilibrium solution, a common alternative approach extends the Harris sheet's analytic form to initialize force-balanced asymmetric simulation set-ups^{27–29}.

A class of exact solutions to the Vlasov equation has been used to develop a simplified (time-stationary, charge-neutral) model of the magnetopause³⁰. More generalized classes of Vlasov–Maxwell solutions exist for the case of sheared magnetic fields in tangential equilibria, where quantities vary only along one dimension, and the magnetic field and bulk velocity are perpendicular to the gradient direction³¹. Recent investigations present methods to obtain exact

Vlasov equilibria for arbitrary asymmetric current layers, where the profiles for the density, temperature, current density and magnetic fields can be specified as input^{32,33}. One equilibrium solution was constructed from a combination of four shifted Maxwellian distributions³⁴. Even in the simplest cases of these tangential equilibria, when treated kinetically, the pressure tensor can become strongly non-gyrotropic as soon as the gradient scale lengths begin to approach the Larmor radius³⁵. Event-specific equilibrium solutions to the Vlasov equation can be determined from spacecraft measurements by fitting the locally observed distribution function to a prescribed analytic form involving a sum of isotropic and crescent-like components³⁶. Reduced Vlasov simulations (for example, ref. ³⁷) have qualitatively reproduced Magnetospheric Multiscale (MMS) spacecraft observations of electron distributions and parallel electric fields at electron spatial scales during asymmetric reconnection with sharp density and temperature gradients³⁸. The global-hybrid code 'Vlasiator'³⁹ offers the ability to study how the inclusion of kinetic effects influences even large-scale magnetospheric dynamical processes^{40,41}. As demonstrated by these studies' successful implementation of analytical and numerical solutions to the Vlasov equation, kinetic theory is applicable from the smallest to the largest scales of the magnetospheric plasma system.

The studies mentioned above have greatly facilitated data-model comparisons between kinetic Vlasov simulations and satellite observations. In particular, discussion is often focused on multi-spacecraft measurements of the electron distribution function f_e and terms appearing in the generalized Ohm's law^{42–46}, such

¹Department of Astronomy, University of Maryland College Park, College Park, MD, USA. ²NASA Goddard Space Flight Center, Greenbelt, MD, USA.

³Department of Physics and Astronomy and the Center for KINETIC Plasma Physics, West Virginia University, Morgantown, WV, USA. ⁴Laboratory for Atmospheric and Space Physics, University of Colorado Boulder, Boulder, CO, USA. ⁵Blackett Laboratory, Imperial College London, London, UK.

⁶Department of Physics and Astronomy, Dartmouth College, Hanover, NH, USA. ⁷Department of Physics, Catholic University of America, Washington DC, USA. ⁸Universities Space Research Association, Columbia, MD, USA. ⁹Space Science Center, University of New Hampshire, Durham, NH, USA. ¹⁰Southwest Research Institute, San Antonio, TX, USA. ✉e-mail: jason.r.shuster@nasa.gov

as the electron pressure divergence $\nabla \cdot \mathbf{P}_e$, known to play a crucial role in governing the dynamics of the electron diffusion region in both symmetric and asymmetric reconnection configurations^{47–49}. Nevertheless, aside from the present paper and an initial investigation⁵⁰, to our knowledge no direct spacecraft or laboratory measurements of terms in the Vlasov equation have been reported thus far. Because of the sufficiently high-resolution instrumentation on board the MMS four-spacecraft tetrahedron, both spatial and velocity-space variations in f_e are now observable. The Fast Plasma Investigation (FPI)⁵¹, composed of a suite of particle spectrometers on MMS, can successfully resolve spatial gradients of the distribution ∇f_e . This enables direct computation of the spatial gradient term in the electron Vlasov equation, $\mathbf{v} \cdot \nabla f_e$, which can be used to determine how electron populations in velocity-space cooperate to sustain $\nabla \cdot \mathbf{P}_e$ within electron-scale structures⁵⁰.

In this Article, we explore these kinetic origins of $\nabla \cdot \mathbf{P}_e$ by characterizing the MMS measurements of ∇f_e observed in the vicinity of magnetic reconnection operating at Earth's magnetopause. The discovered structures in ∇f_e are compared to a simplified model, which enables both qualitative and quantitative validation of the MMS gradient computations, and provides an intuitive physical interpretation of the ∇f_e signatures. The model is constructed by taking the gradient of a drifting Maxwellian distribution, which yields

$$\nabla f_e = \left[\frac{\nabla n_e}{n_e} + \left(\frac{2(v_{\perp 1} - U_{e\perp 1})}{v_{th}^2} \right) \nabla U_{e\perp 1} + \left(\frac{v_{\parallel}^2 + (v_{\perp 1} - U_{e\perp 1})^2 + v_{\perp 2}^2}{v_{th}^2} - \frac{3}{2} \right) \frac{\nabla T_e}{T_e} \right] f_e \quad (1)$$

where m_e , n_e , $U_{e\perp 1}$ and T_e represent the electron mass, density, bulk velocity in the \perp_1 direction, and temperature, respectively, and $v_{th} = \sqrt{2T_e/m_e}$ is the thermal speed (see Methods for more details). The field-aligned coordinate directions are defined as follows: \parallel is parallel to the magnetic field, \perp_1 is along the $-(\mathbf{U}_e \times \mathbf{B}) \times \mathbf{B}$ direction (approximately the $\mathbf{E} \times \mathbf{B}$ direction), and \perp_2 is along the $-\mathbf{U}_e \times \mathbf{B}$ direction (roughly aligned with \mathbf{E} and ∇n_e for the events considered). ∇f_e denotes the vector quantity $(\partial f_e / \partial x_{\parallel}, \partial f_e / \partial x_{\perp 1}, \partial f_e / \partial x_{\perp 2})$, but for notational convenience we refer to a component of this vector via subscript on the ∇ operator, for example, $\nabla_{\perp 2} f_e \equiv (\nabla f_e)_{\perp 2} = \partial f_e / \partial x_{\perp 2}$. The same techniques for plotting velocity-space slices of the scalar distribution function f_e can be used to visualize each of these scalar components $\nabla_{\parallel} f_e$, $\nabla_{\perp 1} f_e$ and $\nabla_{\perp 2} f_e$. The results of this Article focus on the $\nabla_{\perp 2} f_e$ component because the events chosen for this Article exhibit gradients oriented predominantly along the \perp_2 direction. Thus, we utilize the approximations $\nabla f_e \approx \nabla_{\perp 2} f_e$ and $\mathbf{v} \cdot \nabla f_e \approx v_{\perp 2} \nabla_{\perp 2} f_e$. Note that the velocity-space coordinate \mathbf{v} is not to be confused with the bulk velocity, $\mathbf{U}_e \equiv \frac{1}{n_e} \int \mathbf{v} f_e d^3v$. Throughout the manuscript all temperatures are assumed to be in units of energy (eV), so Boltzmann's constant k is not explicitly written.

Allowing n_e , $U_{e\perp 1}$ and T_e to exhibit a spatial dependence, our model in equation (1) enables direct assessment of how ∇n_e , $\nabla U_{e\perp 1}$ and ∇T_e affect the velocity-space structure of ∇f_e . The density gradient ∇n_e has the simplest effect, modifying $\nabla f_e / f_e$ uniformly in velocity space. The bulk velocity gradient $\nabla U_{e\perp 1}$ gives $\nabla f_e / f_e$ a linear dependence on $v_{\perp 1}$. Finally, the temperature gradient ∇T_e introduces the most complexity to $\nabla f_e / f_e$, resulting in a quadratic dependence on the velocity-space coordinates and a uniform shift. Predictions from the model are illustrated in Fig. 1, which features visualizations of the modelled $\nabla_{\perp 2} f_e$ and $v_{\perp 2} \nabla_{\perp 2} f_e$ velocity-space structures in the $v_{\perp 1} - v_{\perp 2}$ plane with corresponding one-dimensional (1D) cuts for each gradient case (see Methods for additional discussion).

MMS measurements of ∇f_e at the magnetopause

Here we present detailed MMS observations of ∇f_e and $\mathbf{v} \cdot \nabla f_e$, which we compare to the Maxwellian model to guide our interpretation of the kinetic velocity-space features observed within $\nabla \cdot \mathbf{P}_e$ structures

at the magnetopause. Presented first are examples of current layers exhibiting intervals of isolated ∇n_e , $\nabla U_{e\perp 1}$ and ∇T_e , followed by an example current layer with each of these gradients simultaneously present. For each event, the magnitude of $\partial f_e / \partial t$ at the 30-ms cadence of the dual electron spectrometers (DES) is approximately two orders of magnitude smaller than the $\mathbf{v} \cdot \nabla f_e$ and $\mathbf{F} \cdot \nabla f_e$ terms throughout velocity space. The implication is that kinetic balance of the Vlasov equation is achieved mainly by these spatial and velocity-space gradient terms (Methods). Figures 2 to 5 are arranged identically: for each event, panels a–f show an overview of several relevant bulk quantities with a vertical time bar indicating the time at which the distribution slices and cuts featured in panels g–l are taken. Panels d and e use the full temperature tensor, so that $(\nabla \cdot \mathbf{T}_e)_i = \sum_j \partial T_{e,ij} / \partial x_j$ and $(\mathbf{T}_e \cdot \nabla n_e)_i = \sum_j T_{e,ij} (\partial n_e / \partial x_j)$.

Additionally, panel j shows the full scalar product: $\mathbf{v} \cdot \nabla f_e = v_x (\partial f_e / \partial x) + v_y (\partial f_e / \partial y) + v_z (\partial f_e / \partial z)$.

The ∇n_e case. The first case we consider is $\nabla \cdot \mathbf{P}_e \approx \mathbf{T}_e \cdot \nabla n_e$, which is the simplest situation to understand kinetically. When there is only a density gradient ($\nabla n_e \neq 0$, $\nabla U_{e\perp 1} \approx 0$, $\nabla T_e \approx 0$), equation (1) simplifies to $\nabla f_e / f_e = \nabla n_e / n_e$. Figure 2 exhibits a ∇n_e event occurring on 22 October 2015 at 6:03:54.639 universal time (UT) during the first of two reported magnetopause crossings⁵². The structures of $\nabla_{\perp 2} f_e$ and $\mathbf{v} \cdot \nabla f_e$ detected by MMS are shown in Fig. 2g,j, respectively. The Gaussian-like ∇f_e shape and bipolar $\mathbf{v} \cdot \nabla f_e$ structure in the $v_{\perp 2}$ direction are both qualitatively and quantitatively consistent with expectations based on the Maxwellian model (Fig. 2h,k) constructed using the measured n_e , $U_{e\perp 1}$ and T_e observed at this time.

The $\nabla_{\perp 2} f_e > 0$ signature in Fig. 2g–i intuitively means that the phase-space density increases when moving spatially in the direction of the density gradient ∇n_e . Dynamically, the bipolar structure of $\mathbf{v} \cdot \nabla f_e$ results because roughly half of the electrons with $v_{\perp 2} > 0$ ($v_{\perp 2} < 0$) are moving in the direction of increasing (decreasing) density (Fig. 1a–d). Thus, for the Vlasov equation to be satisfied, there must exist a net force that operates to decrease (increase) the phase-space density for $v_{\perp 2} > 0$ ($v_{\perp 2} < 0$). This is precisely the effect of the Lorentz force term $\mathbf{F} \cdot \nabla f_e$. Geometrically, the gradient term ∇f_e is a vector quantity pointing in the direction of increasing phase-space density towards the peak of the distribution. When dotted with the vector force \mathbf{F} , the resulting $\mathbf{F} \cdot \nabla f_e$ must be opposite to $\mathbf{v} \cdot \nabla f_e$ so that $\mathbf{F} \cdot \nabla f_e > 0$ ($\mathbf{F} \cdot \nabla f_e < 0$) for $v_{\perp 2} < 0$ ($v_{\perp 2} > 0$) to balance the velocity-space structure observed in Fig. 2j. For a Maxwellian, terms proportional to $\partial f_e / \partial v_{\perp 2} \propto -v_{\perp 2} f_e$ are capable of effecting this balance because $\partial f_e / \partial v_{\perp 2} > 0$ ($\partial f_e / \partial v_{\perp 2} < 0$) for $v_{\perp 2} < 0$ ($v_{\perp 2} > 0$). In the case of a non-drifting Maxwellian ($U_{e\perp 1} = 0$), the magnetic force term vanishes because the dot product $(\mathbf{v} \times \mathbf{B}) \cdot \nabla f_e = 0$, since rotating a gyrotropic distribution about the magnetic-field direction does not alter the phase-space density (equation (16) in the Methods). For the more general case of a drifting Maxwellian ($U_{e\perp 1} \neq 0$), there is a net contribution from the $(\mathbf{v} \times \mathbf{B}) \cdot \nabla f_e$ term:

$$-\frac{eB}{m_e} \left(v_{\perp 2} \frac{\partial f_e}{\partial v_{\perp 1}} - v_{\perp 1} \frac{\partial f_e}{\partial v_{\perp 2}} \right) = \frac{eB}{T_e} (v_{\perp 2} (v_{\perp 1} - U_{e\perp 1}) - v_{\perp 1} v_{\perp 2}) f_e = -v_{\perp 2} \left(\frac{eU_{e\perp 1} B}{T_e} \right) f_e \quad (2)$$

Thus, even though the dynamical nature of the electric force $-e\mathbf{E}$ and velocity-dependent magnetic force $-e\mathbf{v} \times \mathbf{B}$ differs substantially, the net effect of these forces on the velocity-space ensemble is similar: when dotted with ∇f_e , the terms $E_{\perp 2} \partial f_e / \partial v_{\perp 2}$ and $-(U_{e\perp 1} B) \partial f_e / \partial v_{\perp 2}$ produce bipolar velocity-space structures that can balance the $\mathbf{v} \cdot \nabla f_e$ structure associated with ∇n_e .

The ∇U_e case. Figure 3 shows an event exhibiting a gradient in the bulk velocity ∇U_e . There is a bipolar $\nabla \cdot \mathbf{P}_e$ signature occurring

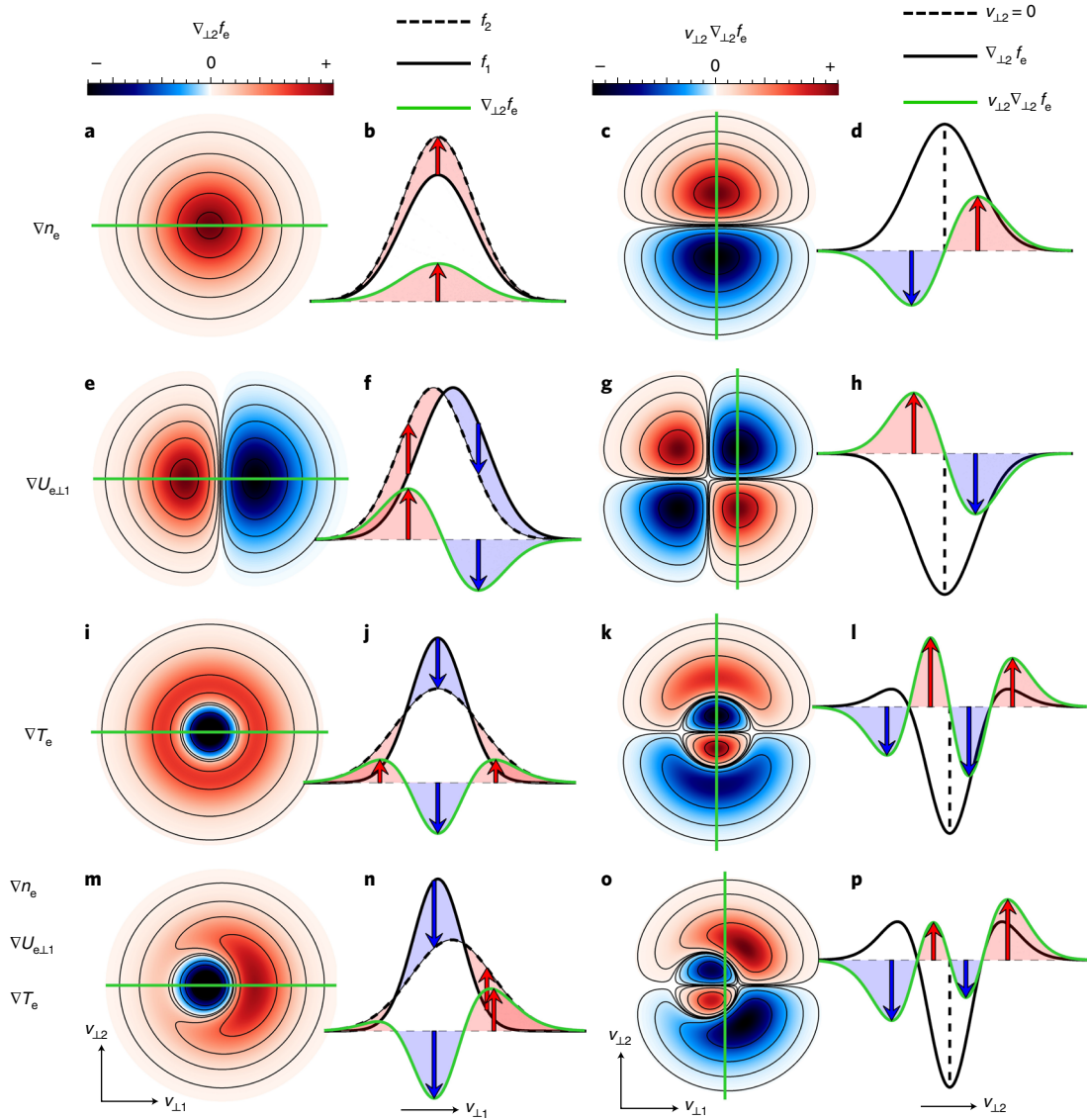


Fig. 1 | Model predictions of ∇f_e and $\mathbf{v} \cdot \nabla f_e$ structures for various plasma gradients. **a–p**, Velocity-space structures in the spatial gradient terms of the Vlasov equation predicted to be the kinetic signatures of plasma gradients in density ∇n_e , bulk velocity $\nabla U_{e\perp 1}$ and temperature ∇T_e . The model distributions illustrate how these gradient structures fundamentally develop between two spatially separated Maxwellian distributions $f_1 = f(\mathbf{x}_1, \mathbf{v})$ and $f_2 = f(\mathbf{x}_2, \mathbf{v})$. Moving spatially from f_1 to f_2 , phase-space density increases (red) or decreases (blue) according to the sign of $\nabla_{\perp 2} f_e$ shown in the first column (**a, e, i, m**). The sets of red and blue arrows in the second column (**b, f, j, n**) indicate how the subtraction ($f_2 - f_1$) generates these $\nabla_{\perp 2} f_e$ structures. The third (**c, g, k, o**) and fourth (**d, h, l, p**) columns show the resulting velocity-space structures as they manifest in the spatial gradient term $\mathbf{v} \cdot \nabla f_e$ when multiplying $\nabla_{\perp 2} f_e$ by $v_{\perp 2}$, which is representative of the gradient ∇f_e structure as experienced by a kinetic electron moving either towards or away from the gradient. **a–p**, $\nabla_{\perp 2} f_e$ and $v_{\perp 2} \nabla_{\perp 2} f_e$ structures associated with a density gradient ∇n_e (**a–d**), bulk velocity gradient $\nabla U_{e\perp 1}$ (**e–h**), temperature gradient ∇T_e (**i–l**) and a combination of these gradients (**m–p**). **a, e, i, m**, 2D $v_{\perp 1}$ – $v_{\perp 2}$ slices of $\nabla_{\perp 2} f_e$. **b, f, j, n**, 1D cuts of f_1 (solid black), f_2 (dashed black) and $\nabla_{\perp 2} f_e$ (green). **c, g, k, o**, 2D $v_{\perp 1}$ – $v_{\perp 2}$ slices of $v_{\perp 2} \nabla_{\perp 2} f_e$. **d, h, l, p**, 1D cuts of $\nabla_{\perp 2} f_e$ (black) and $v_{\perp 2} \nabla_{\perp 2} f_e$ (green).

within roughly 0.3 s of 18:19:23.8 UT on 1 October 2016. Spatial gradients are particularly well-resolved because the average spacecraft separation was 6.42 km at this time, with only 4.88 km separating MMS 2 and MMS 3. The density and temperature gradients were relatively small compared to the other events discussed in this study. As a result, the maximum $\nabla \cdot \mathbf{P}_e$ for this event is only $\sim 2 \text{ pPa km}^{-1}$ (Fig. 3e). At the time of maximum $|\nabla U_e|$, contributions from both ∇n_e and ∇T_e vanish. Nevertheless, there is a strong spatial gradient in the bulk electron velocity at this time, which is manifest in the ∇f_e distribution observed by MMS (Fig. 3g). This prominent bipolar $\nabla_{\perp 2} f_e$ signature along the $v_{\perp 1}$ direction and its corresponding

quadrupolar $\mathbf{v} \cdot \nabla f_e$ structure (Fig. 3j) are consistent with the model results in the case of a non-zero $\nabla U_{e\perp 1}$ (compare to Fig. 3h,k).

Although $\nabla U_{e\perp 1}$ notably alters the observed kinetic structure of ∇f_e , the net $\nabla \cdot \mathbf{P}_e$ signature is independent of ∇U_e because \mathbf{P}_e is independent of \mathbf{U}_e , thus ∇U_e does not appear in the definition of the pressure divergence: $\nabla \cdot \mathbf{P}_e = T_e \cdot \nabla n_e + n_e \nabla \cdot T_e$. Considering the structure of the $\mathbf{v} \cdot \nabla f_e$ signature in Fig. 1g,h, the velocity-weighted integrand $v_{\perp 2}(\mathbf{v} \cdot \nabla f_e)$ retains its quadrupolar symmetry and thus, upon integration, the net contribution to $(\nabla \cdot \mathbf{P}_e)_{\perp 2}$ will be zero because each positive (red) region of the $\mathbf{v} \cdot \nabla f_e$ structure in velocity space will cancel with a neighbouring negative (blue) region

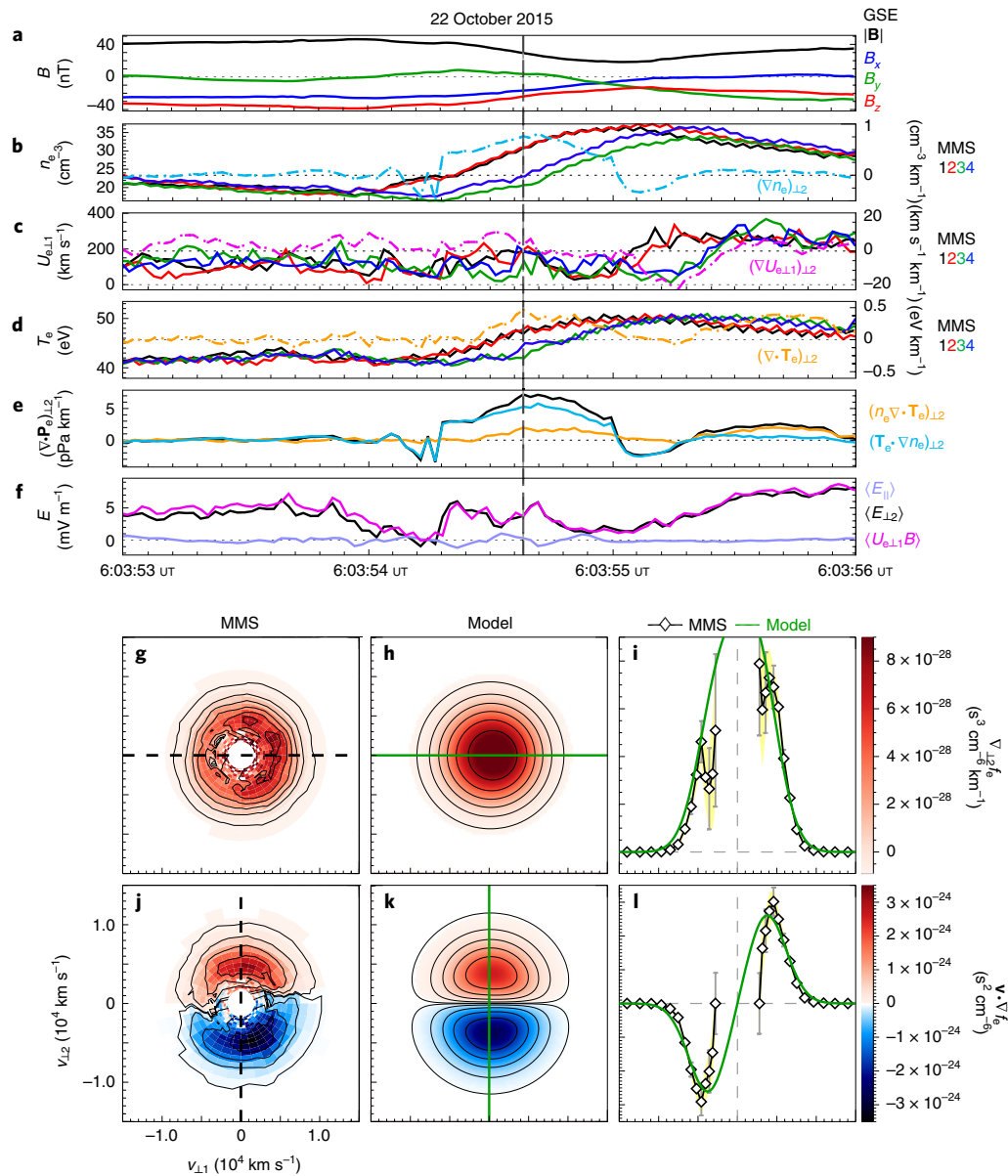


Fig. 2 | MMS observations of unipolar $\nabla_{\perp 2} f_e$ and bipolar $\mathbf{v} \cdot \nabla f_e$ for a density gradient ∇n_e . MMS observations and model predictions of the unipolar electron phase-space density gradient $\nabla_{\perp 2} f_e$ and bipolar $\mathbf{v} \cdot \nabla f_e$ distribution within a magnetopause current layer containing primarily a density gradient ∇n_e . **a**, Magnetic field magnitude $|B|$ (black) and components B_x (blue), B_y (green) and B_z (red) from MMS 1 in geocentric solar ecliptic (GSE) coordinates. **b–d**, Measurements of the electron density n_e (**b**), bulk velocity $U_{e\perp 1}$ (**c**) and temperature T_e (**d**) from all four MMS spacecraft (MMS 1, 2, 3 and 4 in black, red, green and blue, respectively) with corresponding gradient components $(\nabla n_e)_{\perp 2}$ (**b**, aqua), $(\nabla U_{e\perp 1})_{\perp 2}$ (**c**, magenta) and $(\nabla T_e)_{\perp 2}$ (**d**, orange) included in each panel (the right axis displays units for the gradient quantities). **e**, Density gradient $(n_e \nabla \cdot \mathbf{T}_e)_{\perp 2}$ (black) and temperature gradient $(T_e \cdot \nabla n_e)_{\perp 2}$ (blue) terms contributing to the \perp_2 component of the electron pressure divergence $(\nabla \cdot \mathbf{P}_e)_{\perp 2}$. **f**, Four-spacecraft averages of the \perp_2 components of the electric-field terms $\langle E_{\perp 2} \rangle$ (black), $\langle U_{e\perp 1} B \rangle$ (magenta) and the parallel electric field $\langle E_{\parallel} \rangle$ (purple). **g–l**, MMS measurements of $\nabla_{\perp 2} f_e$ (**g**) and $\mathbf{v} \cdot \nabla f_e$ (**j**) at 6:03:54.639 UT (indicated by the vertical dashed line in **a–f**), and the corresponding Maxwellian model distributions of $\nabla_{\perp 2} f_e$ (**h**) and $\mathbf{v} \cdot \nabla f_e$ (**k**) computed using the average n_e , $U_{e\perp 1}$ and T_e at this time. The absence of electron counts near $|\mathbf{v}| \lesssim 2,000$ km s⁻¹ in the MMS distributions (**g**) is due to the subtraction of low-energy photoelectron contamination⁵⁵. **i, l**, 1D cuts for the MMS (black diamonds) and model (green) distributions of $\nabla_{\perp 2} f_e$ along $v_{\perp 1}$ (**i**) and $\mathbf{v} \cdot \nabla f_e$ along $v_{\perp 2}$ (**l**) for quantitative comparison. The colour scales specify both the 2D distribution colour range and the 1D cut range for that row. Error bars for the MMS data (indicated by grey bars with light yellow background) show the uncertainties in the gradient distribution measurements computed using a Monte Carlo resampling technique based on the standard deviations σ_{f_e} provided for the four spacecraft phase-space density f_e data⁵⁶. The dashed grey lines show the plot origin at (0, 0).

(equation (9) in the Methods). This cancellation does not happen for ∇f_e in the ∇n_e case (Fig. 2j), because there the second multiplication by $v_{\perp 2}$ in the velocity-weighted term $v_{\perp 2}(\mathbf{v} \cdot \nabla f_e)$ flips the sign of the negative $\mathbf{v} \cdot \nabla f_e$ in the $v_{\perp 2} < 0$ region, resulting in a positive contribution to $\nabla \cdot \mathbf{P}_e$ throughout velocity space.

Unlike the case of a density gradient, here the Maxwellian distribution cannot satisfy the steady-state Vlasov equation in the case of a $\nabla_{\perp 2} U_{e\perp 1}$ bulk velocity gradient. For this case, equation (1) simplifies to $\nabla f_e / f_e = 2(v_{\perp 1} - U_{e\perp 1}) \nabla U_{e\perp 1} / v_{\text{th}}^2$. Thus, the Vlasov equation becomes

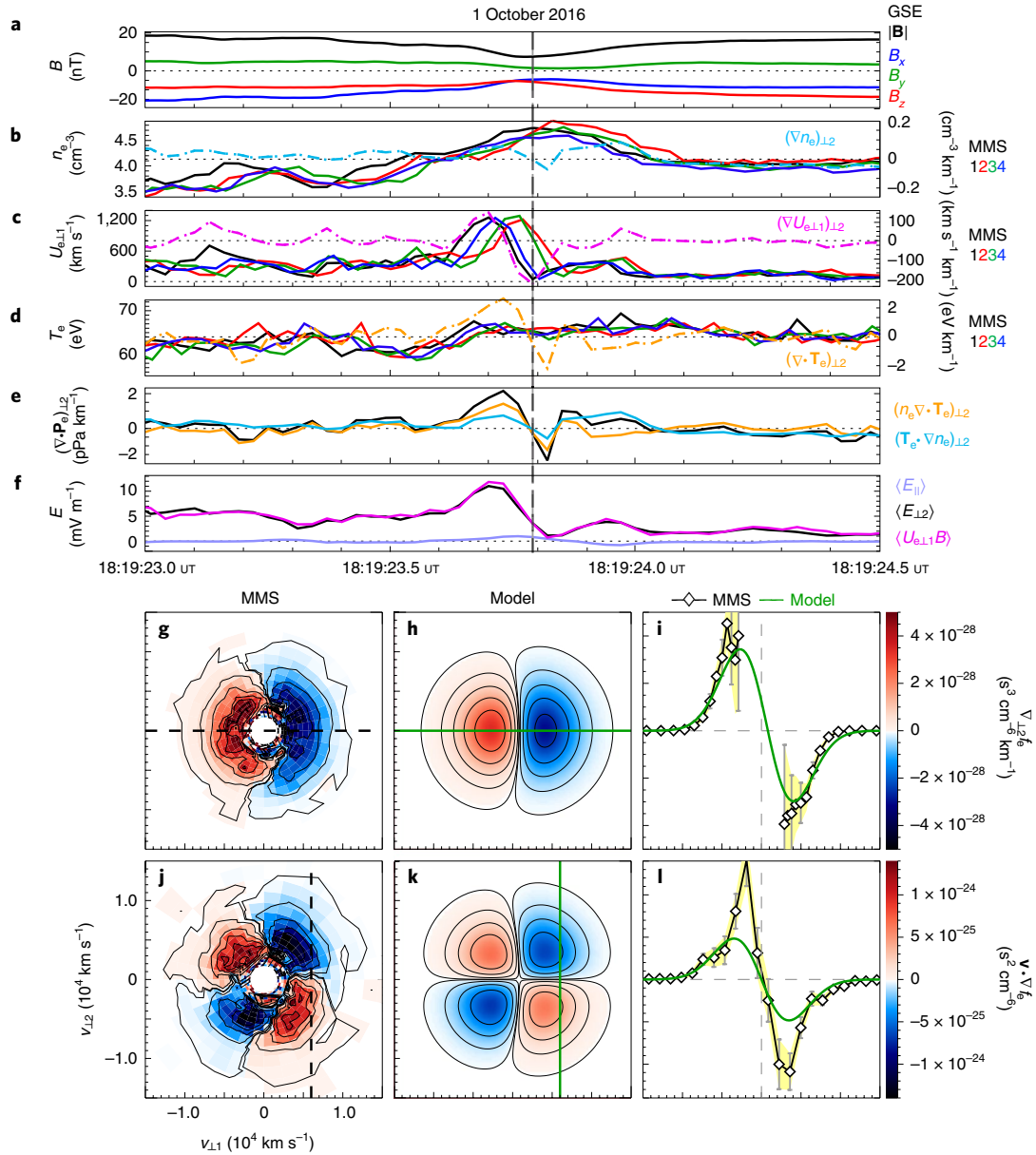


Fig. 3 | MMS observations of bipolar $\nabla_{\perp}f_e$ and quadrupolar $\mathbf{v} \cdot \nabla f_e$ for a velocity gradient ∇U_e . MMS observations and model predictions featuring an electron phase-space density gradient $\nabla_{\perp}f_e$ with a bipolar structure along the v_{\perp} direction and resulting quadrupolar $\mathbf{v} \cdot \nabla f_e$ distribution within a magnetopause current layer exhibiting a bulk velocity gradient ∇U_e . **a**, Magnetic field magnitude $|B|$ (black) and components B_x (blue), B_y (green) and B_z (red) from MMS 1 in GSE coordinates. **b–d**, Measurements of the electron density n_e (**b**), bulk velocity $U_{e\perp 1}$ (**c**) and temperature T_e (**d**) from all four MMS spacecraft (MMS 1, 2, 3 and 4 in black, red, green and blue, respectively) with corresponding gradient components $(\nabla n_e)_{\perp 2}$ (**b**, aqua), $(\nabla U_{e\perp 1})_{\perp 2}$ (**c**, magenta) and $(\nabla T_e)_{\perp 2}$ (**d**, orange) included in each panel (the right axis displays units for the gradient quantities). **e**, Density gradient $(T_e \cdot \nabla n_e)_{\perp 2}$ (aqua) and temperature gradient $(n_e \nabla \cdot T_e)_{\perp 2}$ (orange) terms contributing to the \perp_2 -component of the electron pressure divergence $(\nabla \cdot \mathbf{P}_e)_{\perp 2}$ (black). **f**, Four-spacecraft averages of the \perp_2 components of the electric-field terms $\langle E_{\perp 2} \rangle$ (black), $\langle U_{e\perp 1} B \rangle$ (magenta) and the parallel electric field $\langle E_{\parallel} \rangle$ (purple). **g–l**, MMS measurements of $\nabla_{\perp}f_e$ (**g**) and $\mathbf{v} \cdot \nabla f_e$ (**j**) at 18:19:23.790 UT (indicated by the vertical dashed line in the panels above), and the corresponding Maxwellian model distributions of $\nabla_{\perp}f_e$ (**h**) and $\mathbf{v} \cdot \nabla f_e$ (**k**) computed using the average n_e , $U_{e\perp 1}$ and T_e at this time. The absence of electron counts near $|\mathbf{v}| \lesssim 2,000 \text{ km s}^{-1}$ in the MMS distributions (**g,j**) is due to the subtraction of low-energy photoelectron contamination⁵⁵. **i,l**, 1D cuts for the MMS (black diamonds) and model (green) distributions of $\nabla_{\perp}f_e$ along $v_{\perp 1}$ (**i**) and $\mathbf{v} \cdot \nabla f_e$ along $v_{\perp 2}$ (**l**) for quantitative comparison. The colour scales specify both the 2D distribution colour range and the 1D cut range for that row. Error bars for the MMS data (indicated by grey bars with light yellow background) show the uncertainties in the gradient distribution measurements computed using a Monte Carlo resampling technique based on the standard deviations σ_{f_e} provided for the four spacecraft phase-space density f_e data⁵⁶. The dashed grey lines show the plot origin at (0, 0).

$$v_{\perp 2} \frac{m_e (v_{\perp 1} - U_{e\perp 1})}{T_e} \nabla_{\perp 2} U_{e\perp 1} f_e - \frac{e E_{\perp 2}}{m_e} \frac{\partial f_e}{\partial v_{\perp 2}} - \frac{e B}{m_e} \left(v_{\perp 2} \frac{\partial f_e}{\partial v_{\perp 1}} - v_{\perp 1} \frac{\partial f_e}{\partial v_{\perp 2}} \right) = 0$$

$$v_{\perp 2} (v_{\perp 1} - U_{e\perp 1}) (m_e \nabla_{\perp 2} U_{e\perp 1}) + v_{\perp 2} e (E_{\perp 2} - U_{e\perp 1} B) = 0 \quad (4)$$

(3) where it is apparent that the quadrupolar velocity dependence $v_{\perp 2} (v_{\perp 1} - U_{e\perp 1})$ cannot be balanced by the velocity-space gradient term (only proportional to $v_{\perp 2}$) when f_e is assumed to be Maxwellian.

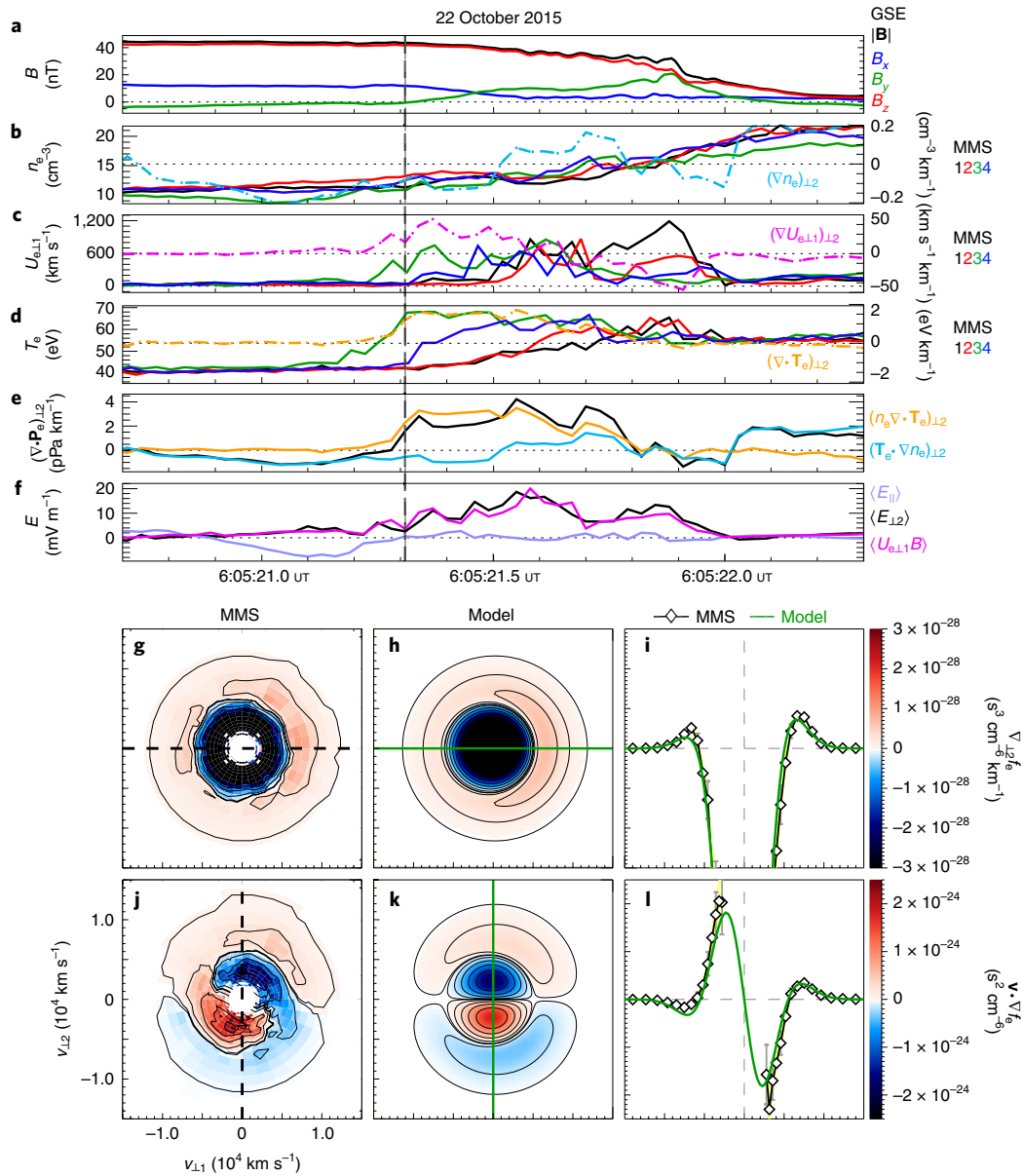


Fig. 4 | MMS observations of ring-shaped $\nabla_{12}f_e$ and $\mathbf{v} \cdot \nabla f_e$ for a temperature gradient ∇T_e . MMS observations and model predictions exhibiting a ring structure in the electron phase-space density gradient $\nabla_{12}f_e$ and corresponding quadrupolar $\mathbf{v} \cdot \nabla f_e$ distribution along the v_{12} direction within a magnetopause current layer supported primarily by a temperature gradient ∇T_e . **a**, Magnetic field magnitude $|B|$ (black) and components B_x (blue), B_y (green) and B_z (red) from MMS 1 in GSE coordinates. **b–d**, Measurements of the electron density n_e (**b**), bulk velocity $U_{e, \perp 1}$ (**c**) and temperature T_e (**d**) from all four MMS spacecraft (MMS 1, 2, 3 and 4 in black, red, green and blue, respectively) with corresponding gradient components $(\nabla n_e)_{\perp 2}$ (**b**, aqua), $(\nabla U_{e, \perp 1})_{\perp 2}$ (**c**, magenta) and $(\nabla T_e)_{\perp 2}$ (**d**, orange) included in each panel (the right axis displays units for the gradient quantities). **e**, Density gradient $(T_e \cdot \nabla n_e)_{\perp 2}$ (aqua) and temperature gradient $(n_e \nabla \cdot T_e)_{\perp 2}$ (orange) terms contributing to the \perp_2 component of the electron pressure divergence $(\nabla \cdot P_e)_{\perp 2}$ (black). **f**, Four-spacecraft averages of the \perp_2 components of the electric-field terms $\langle E_{12} \rangle$ (black), $\langle U_{e, \perp 1} B \rangle$ (magenta) and the parallel electric field $\langle E_{\parallel} \rangle$ (purple). **g–i**, MMS measurements of $\nabla_{12}f_e$ (**g**) and $\mathbf{v} \cdot \nabla f_e$ (**j**) at 6:05:21.310 UT (indicated by the vertical dashed line in the panels above), and the corresponding Maxwellian model distributions of $\nabla_{12}f_e$ (**h**) and $\mathbf{v} \cdot \nabla f_e$ (**k**) computed using the average n_e , $U_{e, \perp 1}$ and T_e at this time. The absence of electron counts near $|\mathbf{v}| \lesssim 2,000 \text{ km s}^{-1}$ in the MMS distributions (**g**, **j**) is due to the subtraction of low-energy photoelectron contamination⁵⁵. **i**, **l**, 1D cuts for the MMS (black diamonds) and model (green) distributions of $\nabla_{12}f_e$ along v_{11} (**i**) and $\mathbf{v} \cdot \nabla f_e$ along v_{12} (**l**) for quantitative comparison. The colour scales specify both the 2D distribution colour range and the 1D cut range for that row. For **g–i**, the scale is saturated to emphasize the positive $\nabla_{12}f_e > 0$ ring structure. Error bars for the MMS data (indicated by grey bars with light yellow background) show the uncertainties in the gradient distribution measurements computed using a Monte Carlo resampling technique based on the standard deviations σ_{f_e} provided for the four spacecraft phase-space density f_e data⁵⁶. The dashed grey lines show the plot origin at (0, 0).

The ∇T_e case. On 22 October 2015 during the second of two reported magnetopause crossings⁵², there is an interval near 6:05:21 UT where $\nabla \cdot P_e \approx n_e \nabla \cdot T_e$ (Fig. 4). MMS observes a ring-structured $\nabla_{12}f_e$ (Fig. 4g), which results in a tripolar 1D cut (Fig. 4i), with

$\nabla_{12}f_e < 0$ for velocities satisfying $(v_{11}^2 + v_{12}^2) < v_0^2$ (inner blue negative region), while $\nabla_{12}f_e > 0$ for $(v_{11}^2 + v_{12}^2) > v_0^2$ (outer red positive region), where v_0 specifies the radius in this slice of velocity space for which $\nabla_{12}f_e = 0$. From the model ∇f_e in equation (1), considering

the slice with $v_{\parallel}=0$, no bulk velocity shift ($U_{e\perp 1}=0$), and setting both the ∇n_e and $\nabla U_{e\perp 1}$ terms to zero, we can solve for v_0 , which comes out to be slightly larger than the local thermal speed:

$$\frac{\nabla f_e}{f_e} = \left(\frac{v_0^2}{v_{th}^2} - \frac{3}{2} \right) \frac{\nabla T_e}{T_e} = 0 \rightarrow v_0 = \sqrt{\frac{3T_e}{m_e}} = v_{th} \sqrt{\frac{3}{2}} \approx 1.2 v_{th} \quad (5)$$

The reason for this ring structure in ∇f_e can be explained intuitively by noting a Maxwellian's temperature dependence: $f_e \propto T_e^{-3/2} \exp(-m_e v^2/2T_e)$. Increasing the temperature therefore affects the velocity distribution in two ways, by increasing its spread (that is, heating) and decreasing the distribution's maximum at its centre so that the total density of the distribution remains unaffected. Thus, increasing the distribution's spread results in the $\nabla_{\perp 2} f_e > 0$ positive (red) ring region of velocity space, while depleting the distribution's maximum results in the negative $\nabla_{\perp 2} f_e < 0$ (blue) core (Fig. 1i,j). This structure indicates that phase-space density decreases (increases) for $|v| \lesssim v_{th}$ ($|v| \gtrsim v_{th}$) when moving spatially in the $\pm \perp_2$ direction. Consequently, the dynamic measure of $\mathbf{v} \cdot \nabla f_e \approx v_{\perp 2} \nabla_{\perp 2} f_e$ becomes quadrupolar along the $v_{\perp 2}$ direction (Fig. 1k,l). MMS observations of this structure in $\mathbf{v} \cdot \nabla f_e$ (Fig. 4j) agree well with the Maxwellian model (Fig. 4k). There is a slight tilt of the quadrupolar structure in the MMS distribution (Fig. 4j) resulting from a non-zero \perp_1 gradient term $\nabla_{\perp 1} f_e$, although the dominant gradient contribution is still provided by $\nabla_{\perp 2} f_e$. The meaning of this multi-component $\mathbf{v} \cdot \nabla f_e$ structure becomes apparent when we consider each half of velocity space corresponding to the sign of $v_{\perp 2}$. First considering subthermal electrons with $|v| < v_{th}$, those that move in the direction of increasing (decreasing) temperature encounter decreased (increased) phase-space density because $T_e^{-3/2}$ decreases (increases) as T_e increases (decreases). The situation is reversed for superthermal electrons with $|v| > v_{th}$ due to the $\exp(-m_e v^2/2T_e)$ dependence: electrons moving towards (away from) the gradient with $v_{\perp 2} > 0$ ($v_{\perp 2} < 0$) encounter a hotter (colder) distribution and thus enter a region of higher (lower) phase-space density.

As with the ∇U_e case, a Maxwellian distribution cannot satisfy the steady-state Vlasov equation in the ∇T_e case. This becomes apparent after inserting the appropriate form of $\mathbf{v} \cdot \nabla f_e$ into the Vlasov equation and simplifying:

$$\left(\frac{v^2}{v_{th}^2} - \frac{3}{2} \right) \nabla_{\perp 2} T_e + e(E_{\perp 2} - U_{e\perp 1} B) = 0 \quad (6)$$

Thus, $(E_{\perp 2} - U_{e\perp 1} B)$ cannot be chosen to make this equation true for all \mathbf{v} , because this force term is independent of the velocity-space coordinates. The velocity-space derivative of a Maxwellian yields at most terms of order v , which cannot account for the additional v^2 dependence appearing due to the ∇T_e term. The inability of a Maxwellian to provide kinetic equilibrium in the case of a temperature gradient is consistent with the MMS observations of non-Maxwellian populations, such as the electron crescent distributions that were reported in this ∇T_e interval⁵² and in the event addressed in the next section⁵⁰.

Combination of ∇n_e , ∇U_e and ∇T_e gradients. The ∇f_e structure associated with the thin current sheet event occurring on 23 December 2016 reported previously⁵⁰ results from a combination of ∇n_e , $\nabla U_{e\perp 1}$ and ∇T_e gradient effects cooperating within the layer (Fig. 5). At the time of maximum $\nabla \cdot \mathbf{P}_e$, the temperature divergence term $(n_e \nabla \cdot \mathbf{T}_e)_{\perp 2}$ surpasses the density gradient term $(\mathbf{T}_e \cdot \nabla n_e)_{\perp 2}$ (Fig. 5e) and thus ∇f_e acquires a ring structure. Slightly afterwards, $\nabla U_{e\perp 1}$ also reaches its maximum (Fig. 5c) near 2:53:10.311 UT, the time at which MMS observed the ∇f_e and $\mathbf{v} \cdot \nabla f_e$ structures shown in Fig. 5g,j. These velocity-space features qualitatively agree with the corresponding model distributions shown in Fig. 5h,k. The bipolar

crescent structure in $\nabla_{\perp 2} f_e$ and asymmetric skewed quadrupole distribution of $\mathbf{v} \cdot \nabla f_e$ result mainly from the coexisting bulk velocity and temperature gradients. In this case, the density gradient affects the magnitude of ∇f_e , but does not visibly alter its structure.

The difference in magnitude between the MMS distributions and model distributions probably results because the velocity distributions f_e at this time are non-Maxwellian, and the current layer is noticeably smaller than the spacecraft separation (Fig. 5c), which introduces uncertainty into the accuracy of the gradient computation. Owing to asymmetries in the non-gyrotropic crescent distribution⁵⁰, the off-diagonal components of the pressure tensor are small yet finite (roughly 5% of the diagonal components), which may also contribute to the quantitative difference between the modelled and measured $\mathbf{v} \cdot \nabla f_e$ at this time. Nevertheless, the qualitative agreement of the Maxwellian model, which reproduces the predominant skewed and quadrupolar velocity-space features, still offers useful insight into how the non-zero $\nabla \cdot \mathbf{P}_e$ results from the behaviour of electrons within this thin current layer. Each of the four regions of $\mathbf{v} \cdot \nabla f_e$ (Fig. 5j,k) contribute to $\nabla \cdot \mathbf{P}_e$. When multiplying by the additional factor of $v_{\perp 2}$, the two regions in $\mathbf{v} \cdot \nabla f_e$ for $v_{\perp 2} < 0$ reverse their signs in the velocity-weighted integrand $v_{\perp 2}(\mathbf{v} \cdot \nabla f_e)$. Thus, the two outer crescent regions of velocity space contribute positively to $\nabla \cdot \mathbf{P}_e$, while the inner lower-velocity regions contribute negatively. Because of the velocity weighting, the higher-velocity crescent regions dominate the integration for this case, resulting in the observed $(\nabla \cdot \mathbf{P}_e)_{\perp 2} > 0$ (Fig. 5e).

Outlook

The qualitative and often quantitative agreement between the MMS measurements of ∇f_e and the Maxwellian model gives confidence to our kinetic interpretation of these observations and indicates the accuracy of the MMS multi-spacecraft phase-space density gradient measurements. Although we focus on the steady-state Vlasov equation requiring that $\mathbf{v} \cdot \nabla f_e$ and $(\mathbf{F}/m_e) \cdot \nabla f_e$ balance throughout velocity space, we note that $\partial f_e / \partial t$ may become significant with increased temporal and velocity-space resolution (even higher than is provided by the DES), which is important for non-equilibrium events and the application to wave-particle interactions when the relevant timescales are much less than 30 ms (that is, when the wave frequency is much greater than ~ 100 Hz). Further work is needed to compute the velocity-space gradient ∇f_e term using MMS measurements to observationally verify its ability to balance the types of spatial gradient $\mathbf{v} \cdot \nabla f_e$ structure reported here. Provided that $(\mathbf{F}/m_e) \cdot \nabla f_e$ could be sufficiently resolved by MMS and future spacecraft missions, these results point towards an approach for inferring local spatial gradients, and consequently moments such as the pressure divergence, directly from single spacecraft ∇f_e vector measurements for both steady-state and temporally evolving systems.

The MMS measurements of bulk plasma gradients and their effect on the velocity-space structure of ∇f_e reported here may also provide observational constraints useful to both analytic and numerical methods of solving the Vlasov-Maxwell system in the presence of velocity and temperature gradients^{53,54}. Although our Maxwellian gradient model in equation (1) does not satisfy the Vlasov equation exactly for these cases, the qualitative agreement between our model and the MMS measurements of the $\mathbf{v} \cdot \nabla f_e$ structures throughout velocity space nevertheless suggests a natural way for future studies to improve our model: if the local distribution f_e were instead modelled as a superposition of two Maxwellians, f_{e1} and f_{e2} , constructed from the plasma parameters taken on either side of the gradient layer, the spatial gradient term $\mathbf{v} \cdot \nabla f_e$ would be largely preserved (that is, consistent with the gradient structures illustrated in Fig. 1) while also allowing for a more self-consistent non-Maxwellian velocity-space structure to develop in the $(\mathbf{F}/m_e) \cdot \nabla f_e$ term. This suggested improvement, $f_e = f_{e1} + f_{e2}$, is reminiscent of the exact Vlasov-Maxwell equilibria for asymmetric

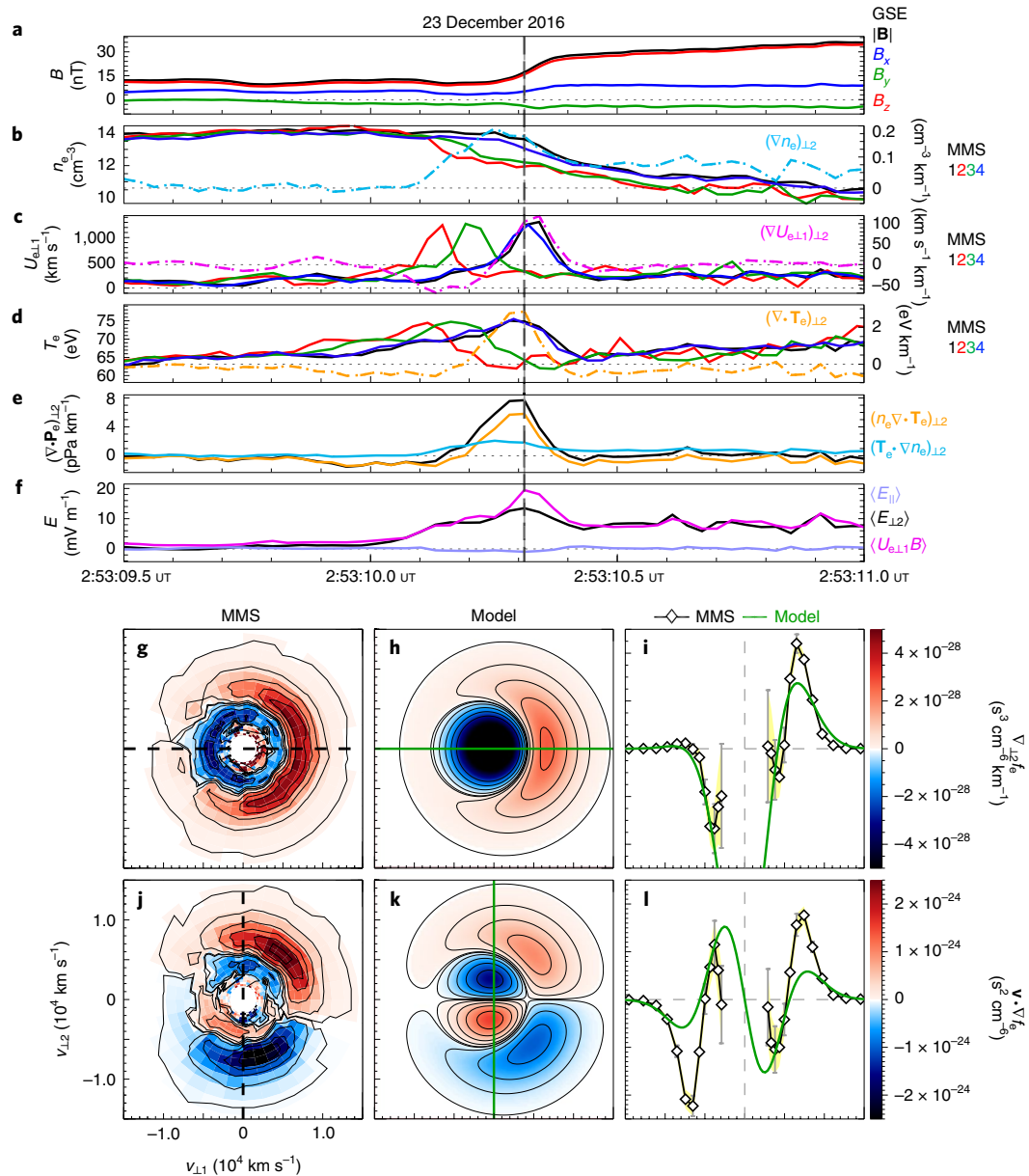


Fig. 5 | MMS observations of crescent-shaped $\nabla_{\perp} f_e$ and $\mathbf{v} \cdot \nabla f_e$ for a combination of gradients. MMS observations and model predictions of a bipolar crescent structure in $\nabla_{\perp} f_e$ and skewed quadrupolar structure in $\mathbf{v} \cdot \nabla f_e$ which develop due to the combination of density, bulk velocity and temperature gradients that support this electron-scale current layer at the magnetopause. **a**, Magnetic field magnitude $|B|$ (black) and components B_x (blue), B_y (green) and B_z (red) from MMS 1 in GSE coordinates. **b–d**, Measurements of the electron density n_e (**b**), bulk velocity $U_{e,1}$ (**c**) and temperature T_e (**d**) from all four MMS spacecraft (MMS 1, 2, 3 and 4 in black, red, green and blue, respectively) with corresponding gradient components $(\nabla n_e)_{\perp 2}$ (**b**, aqua), $(\nabla U_{e,1})_{\perp 2}$ (**c**, magenta) and $(\nabla T_e)_{\perp 2}$ (**d**, orange) included in each panel (the right axis displays units for the gradient quantities). **e**, Density gradient $(T_e \cdot \nabla n_e)_{\perp 2}$ (aqua) and temperature gradient $(n_e \nabla \cdot T_e)_{\perp 2}$ (orange) terms contributing to the \perp_2 component of the electron pressure divergence $(\nabla \cdot \mathbf{P}_e)_{\perp 2}$ (black). **f**, Four-spacecraft averages of the \perp_2 components of the electric-field terms $\langle E_{\perp 2} \rangle$ (black), $\langle U_{e,1} B \rangle$ (magenta) and the parallel electric field $\langle E_{\parallel} \rangle$ (purple). **g–l**, MMS measurements of $\nabla_{\perp} f_e$ (**g**) and $\mathbf{v} \cdot \nabla f_e$ (**j**) at 2:53:10.311 UT (indicated by the vertical dashed line in the panels above) and the corresponding Maxwellian model distributions of $\nabla_{\perp} f_e$ (**h**) and $\mathbf{v} \cdot \nabla f_e$ (**k**) computed using the average n_e , $U_{e,1}$ and T_e at this time. The absence of electron counts near $|\mathbf{v}| \lesssim 2,000 \text{ km s}^{-1}$ in the MMS distributions (**g**, **j**) is due to the subtraction of low-energy photoelectron contamination⁵⁵. **i**, **l**, 1D cuts for the MMS (black diamonds) and model (green) distributions of $\nabla_{\perp} f_e$ along $v_{\perp 1}$ (**i**) and $\mathbf{v} \cdot \nabla f_e$ along $v_{\perp 2}$ (**l**) for quantitative comparison. The colour scales specify both the 2D distribution colour range and the 1D cut range for that row. Error bars for the MMS data (indicated by grey bars with light yellow background) show the uncertainties in the gradient distribution measurements computed using a Monte Carlo resampling technique based on the standard deviations σ_{f_e} provided for the four spacecraft phase-space density f_e data⁵⁶. The dashed grey lines show the plot origin at (0, 0).

current sheets, which require a combination of four drifting Maxwellians³⁴. Comparing $\mathbf{v} \cdot \nabla f_e$ measured by MMS to the modelled $\mathbf{v} \cdot \nabla f_0$ (where f_0 is a drifting Maxwellian constructed using the locally observed moments) in this fashion enables us to gain insight

into the higher-order non-gyrotropic corrections to f_0 that would be needed to satisfy the full Vlasov equation.

The methodology and characterization of ∇f_e reported here may be applied to more complicated electron diffusion region

events, such as those reported previously^{13,15}, provided that the four-spacecraft gradient approximation is valid for the time interval of interest. In particular, our approach may also be used to characterize the velocity-space structure of the off-diagonal contribution to the pressure divergence via the following integral relationship (equation (9) in the Methods) when the inertial term is sufficiently small:

$$m_e \int v_i \left(v_j \frac{\partial f_e}{\partial x_j} \right) d^3 v = \frac{\partial P_{e,ij}}{\partial x_j} \quad (7)$$

Thus, the quantity $v_j \partial f_e / \partial x_j$ is of particular interest to future studies seeking to identify which populations of electrons in velocity space produce a net off-diagonal contribution to the electron pressure divergence. Our results are relevant for understanding kinetically how the electron pressure divergence $\nabla \cdot \mathbf{P}_e$ operates in velocity space to self-consistently sustain the reconnection electric field within the electron diffusion region of magnetic reconnection, as well as other electron-scale dynamics associated with fundamental energization mechanisms throughout Earth's magnetosphere.

Online content

Any methods, additional references, Nature Research reporting summaries, source data, extended data, supplementary information, acknowledgements, peer review information; details of author contributions and competing interests; and statements of data and code availability are available at <https://doi.org/10.1038/s41567-021-01280-6>.

Received: 28 April 2020; Accepted: 28 May 2021;

Published online: 05 July 2021

References

- Vlasov, A. A. On the kinetic theory of an assembly of particles with collective interaction. *J. Phys. (USSR)* **9**, 25–40 (1945).
- Nicholson, D. R. *Introduction to Plasma Theory* (Wiley, 1983).
- Landau, L. D. On the vibrations of the electronic plasma. *J. Phys. (USSR)* **10**, 25–34 (1946).
- Matthaeus, W. H. & Lamkin, S. L. Turbulent magnetic reconnection. *Phys. Fluids* **29**, 2513–2534 (1986).
- Daughton, W. Nonlinear dynamics of thin current sheets. *Phys. Plasmas* **9**, 3668–3678 (2002).
- Sundkvist, D., Retinò, A., Vaivads, A. & Bale, S. D. Dissipation in turbulent plasma due to reconnection in thin current sheets. *Phys. Rev. Lett.* **99**, 025004 (2007).
- Gershman, D. J. et al. Wave–particle energy exchange directly observed in a kinetic Alfvén-branch wave. *Nat. Commun.* **8**, 14719 (2017).
- Viñas, A. F. & Klimas, A. J. Flux-balance Vlasov simulation with filamentation filtration. *J. Comput. Phys.* **375**, 983–1004 (2018).
- Li, T. C., Howes, G., Klein, K., Liu, Y.-H. & TenBarge, J. M. Collisionless energy transfer in kinetic turbulence: field-particle correlations in Fourier space. *J. Plasma Phys.* **85**, 905850406 (2019).
- Chen, C., Klein, K. & Howes, G. Evidence for electron Landau damping in space plasma turbulence. *Nat. Commun.* **10**, 740 (2019).
- Moore, T. E., Burch, J. L. & Torbert, R. B. Magnetic reconnection. *Nat. Phys.* **11**, 611–613 (2015).
- Cassak, P. A. Inside the black box: magnetic reconnection and the magnetospheric multiscale mission. *Space Weather* **14**, 186–197 (2016).
- Burch, J. L. et al. Electron-scale measurements of magnetic reconnection in space. *Science* **352**, aaf2939 (2016).
- Torbert, R. B. et al. Electron-scale dynamics of the diffusion region during symmetric magnetic reconnection in space. *Science* **362**, 1391–1395 (2018).
- Webster, J. M. et al. Magnetospheric multiscale dayside reconnection electron diffusion region events. *J. Geophys. Res. Space Phys.* **123**, 4858–4878 (2018).
- Phan, T. D. et al. Electron magnetic reconnection without ion coupling in Earth's turbulent magnetosheath. *Nature* **557**, 202–206 (2018).
- Hesse, M. & Cassak, P. A. Magnetic reconnection in the space sciences: past, present and future. *J. Geophys. Res. Space Phys.* **125**, e2018JA025935 (2020).
- Roth, M., De Keyser, J. & Kuznetsova, M. M. Vlasov theory of the equilibrium structure of tangential discontinuities in space plasmas. *Space Sci. Rev.* **76**, 251–317 (1996).
- Neukirch, T., Wilson, F. & Allanson, O. Collisionless current sheet equilibria. *Plasma Phys. Control. Fusion* **60**, 014008 (2018).
- Harris, E. G. On a plasma sheath separating regions of oppositely directed magnetic field. *Nuovo Cimento* **23**, 115–121 (1962).
- Chen, L.-J. et al. Evidence of an extended electron current sheet and its neighboring magnetic island during magnetotail reconnection. *J. Geophys. Res. Space Phys.* **113**, A12213 (2008).
- Egedal, J., Daughton, W. & Le, A. Large-scale electron acceleration by parallel electric fields during magnetic reconnection. *Nat. Phys.* **8**, 321–324 (2012).
- Bessho, N., Chen, L.-J., Shuster, J. R. & Wang, S. Electron distribution functions in the electron diffusion region of magnetic reconnection: physics behind the fine structures. *Geophys. Res. Lett.* **41**, 8688–8695 (2014).
- Shuster, J. R. et al. Spatiotemporal evolution of electron characteristics in the electron diffusion region of magnetic reconnection: implications for acceleration and heating. *Geophys. Res. Lett.* **42**, 2586–2593 (2015).
- Wang, S. et al. Electron heating in the exhaust of magnetic reconnection with negligible guide field. *J. Geophys. Res. Space Phys.* **121**, 2104–2130 (2016).
- Yamada, M. et al. Experimental investigation of the neutral sheet profile during magnetic reconnection. *Phys. Plasmas* **7**, 1781–1787 (2000).
- Pritchett, P. L. Collisionless magnetic reconnection in an asymmetric current sheet. *J. Geophys. Res. Space Phys.* **113**, A06210 (2008).
- Daughton, W., Nakamura, T. K. M., Karimabadi, H., Roytershteyn, V. & Loring, B. Computing the reconnection rate in turbulent kinetic layers by using electron mixing to identify topology. *Phys. Plasmas* **21**, 052307 (2014).
- Swisdak, M. et al. Localized and intense energy conversion in the diffusion region of asymmetric magnetic reconnection. *Geophys. Res. Lett.* **45**, 5260–5267 (2018).
- Alpers, W. Steady state charge neutral models of the magnetopause. *Astrophys. Space Sci.* **5**, 425–437 (1969).
- Channell, P. J. Exact Vlasov–Maxwell equilibria with sheared magnetic fields. *Phys. Fluids* **19**, 1541–1545 (1976).
- Mottez, F. Exact nonlinear analytic Vlasov–Maxwell tangential equilibria with arbitrary density and temperature profiles. *Phys. Plasmas* **10**, 2501–2508 (2003).
- Aunai, N., Belmont, G. & Smets, R. First demonstration of an asymmetric kinetic equilibrium for a thin current sheet. *Phys. Plasmas* **20**, 110702 (2013).
- Allanson, O., Wilson, F., Neukirch, T., Liu, Y.-H. & Hodgson, J. D. B. Exact Vlasov–Maxwell equilibria for asymmetric current sheets. *Geophys. Res. Lett.* **44**, 8685–8695 (2017).
- Mottez, F. The pressure tensor in tangential equilibria. *Ann. Geophys.* **22**, 3033–3037 (2004).
- Newman, D. L., Lapenta, G. & Goldman, M. *Dynamics of Electron-scale Current Sheet Wquilibria based on MMS Observations* American Geophysical Union Fall Meeting, eLightning Presentation SM24B-13 (Earth and Space Science Open Archive, 2019); <https://doi.org/10.1002/essoar.10502614.1>
- Newman, D. L., Sen, N. & Goldman, M. V. ‘Reduced’ multidimensional Vlasov simulations, with applications to electrostatic structures in space plasmas. *Phys. Plasmas* **14**, 055907 (2007).
- Holmes, J. C. et al. Structure of electron-scale plasma mixing along the dayside reconnection separatrix. *J. Geophys. Res. Space Phys.* **124**, 8788–8803 (2019).
- Palmroth, M. et al. Vlasov methods in space physics and astrophysics. *Living Rev. Comput. Astrophys.* **4**, 1 (2018).
- von Alfthan, S. et al. Vlasior: first global hybrid-Vlasov simulations of Earth's foreshock and magnetosheath. *J. Atmos. Sol. Terr. Phys.* **120**, 24–35 (2014).
- Hoilijoki, S. et al. Reconnection rates and X line motion at the magnetopause: global 2D-3V hybrid-Vlasov simulation results. *J. Geophys. Res. Space Phys.* **122**, 2877–2888 (2017).
- Vasyliunas, V. M. Theoretical models of magnetic field line merging. *Rev. Geophys.* **13**, 303–336 (1975).
- Viñas, A. F. & Gurgiolo, C. Spherical harmonic analysis of particle velocity distribution function: comparison of moments and anisotropies using cluster data. *J. Geophys. Res. Space Phys.* **114**, A01105 (2009).
- Torbert, R. B. et al. Estimates of terms in Ohm's law during an encounter with an electron diffusion region. *Geophys. Res. Lett.* **43**, 5918–5925 (2016).
- Shuster, J. R. et al. Hodographic approach for determining spacecraft trajectories through magnetic reconnection diffusion regions. *Geophys. Res. Lett.* **44**, 1625–1633 (2017).
- Rager, A. C. et al. Electron crescent distributions as a manifestation of diamagnetic drift in an electron-scale current sheet: magnetospheric multiscale observations using new 7.5-ms fast plasma investigation moments. *Geophys. Res. Lett.* **45**, 578–584 (2018).
- Hesse, M., Neukirch, T., Schindler, K., Kuznetsova, M. & Zenitani, S. The diffusion region in collisionless magnetic reconnection. *Space Sci. Rev.* **160**, 3–23 (2011).
- Hesse, M., Aunai, N., Sibeck, D. & Birn, J. On the electron diffusion region in planar, asymmetric, systems. *Geophys. Res. Lett.* **41**, 8673–8680 (2014).
- Genestreti, K. J. et al. MMS observation of asymmetric reconnection supported by 3-D electron pressure divergence. *J. Geophys. Res. Space Phys.* **123**, 1806–1821 (2018).

50. Shuster, J. R. et al. MMS measurements of the Vlasov equation: probing the electron pressure divergence within thin current sheets. *Geophys. Res. Lett.* **46**, 7862–7872 (2019).
51. Pollock, C. et al. Fast plasma investigation for magnetospheric multiscale. *Space Sci. Rev.* **199**, 331–406 (2016).
52. Phan, T. D. et al. MMS observations of electron-scale filamentary currents in the reconnection exhaust and near the X line. *Geophys. Res. Lett.* **43**, 6060–6069 (2016).
53. Mahajan, S. M. Exact and almost exact solutions to the Vlasov–Maxwell system. *Phys. Fluids B Plasma Phys.* **1**, 43–54 (1989).
54. Klimas, A. J. & Viñas, A. F. Open-boundary spectral and flux-balance Vlasov simulation. *J. Plasma Phys.* **85**, 905850610 (2019).
55. Gershman, D. J. et al. Spacecraft and instrument photoelectrons measured by the dual electron spectrometers on MMS. *J. Geophys. Res. Space Phys.* **122**, 11548–11558 (2017).
56. Gershman, D. J., Dorelli, J. C., F-Viñas, A. & Pollock, C. J. The calculation of moment uncertainties from velocity distribution functions with random errors. *J. Geophys. Res. Space Phys.* **120**, 6633–6645 (2015).

Publisher's note Springer Nature remains neutral with regard to jurisdictional claims in published maps and institutional affiliations.

© The Author(s), under exclusive licence to Springer Nature Limited 2021

Methods

Computing phase-space density gradients with FPI. For this study, we consider the Vlasov equation specifying the dynamical evolution of electron phase-space density:

$$\frac{df_e}{dt} = \frac{\partial f_e}{\partial t} + \mathbf{v} \cdot \nabla f_e - \frac{e}{m_e} (\mathbf{E} + \mathbf{v} \times \mathbf{B}) \cdot \nabla f_e = 0 \quad (8)$$

Deriving the electron momentum equation from the first moment of equation (8), the electron pressure divergence $\nabla \cdot \mathbf{P}_e$ originates from the spatial gradient term $\mathbf{v} \cdot \nabla f_e$, as shown by the following integral connection between the kinetic and bulk quantities⁵⁷:

$$m_e \int \mathbf{v} (\mathbf{v} \cdot \nabla f_e) d^3 v = \nabla \cdot \mathbf{P}_e + \nabla \cdot (m_e n_e \mathbf{U}_e \mathbf{U}_e) \quad (9)$$

For the electron-scale current layers considered in this study, the inertial term $\nabla \cdot (m_e n_e \mathbf{U}_e \mathbf{U}_e)$ in equation (9) is typically much smaller than $\nabla \cdot \mathbf{P}_e$ (ref. 50). Commonly observed magnetosheath values for the electron density ($n_e \approx 10 \text{ cm}^{-3}$) and temperature ($T_e \approx 70 \text{ eV}$) with moderate gradients in each quantity ($\nabla n_e \approx 1 \text{ cm}^{-3} \text{ km}^{-1}$ and $\nabla T_e \approx 1 \text{ eV km}^{-1}$) result in pressure gradients of the order of $\sim 1\text{--}10 \text{ pPa km}^{-1}$. However, for typical bulk velocities on the order of $100\text{--}1,000 \text{ km s}^{-1}$ with a gradient $\nabla U_e \approx 10 (\text{km s}^{-1}) \text{ km}^{-1}$, the range of values for the inertial term is one to two orders of magnitude smaller, roughly $0.01\text{--}0.1 \text{ pPa km}^{-1}$. If the electron flows and spatial gradients are strong enough (for example, $U_e \approx 1,000 \text{ km s}^{-1}$ combined with a sharp bulk velocity gradient $\nabla U_e \approx 100 (\text{km s}^{-1}) \text{ km}^{-1}$), then the magnitude of the inertial term can begin to approach 1.0 pPa km^{-1} . Consequently, because $\nabla \cdot \mathbf{P}_e$ usually dominates $\nabla \cdot (m_e n_e \mathbf{U}_e \mathbf{U}_e)$, the computation of ∇f_e as a function of \mathbf{v} gives a direct measure quantifying how electron populations in velocity space kinetically contribute to the net pressure gradient. We note that, if the inertial term were to surpass the pressure divergence (for example, in electron diffusion regions or separatrixes), then ∇f_e would still offer an important kinetic perspective into the electron populations that support $\nabla \cdot (m_e n_e \mathbf{U}_e \mathbf{U}_e)$.

To compute ∇f_e and $\mathbf{v} \cdot \nabla f_e$, we utilize a recently developed technique⁵⁰. The method extends the usual multi-spacecraft technique for computing linear spatial gradients of bulk quantities, for example, as in ref. 58, to the velocity-space measurements obtained by FPI's DES. The computation is performed in geocentric solar ecliptic (GSE) coordinates before rotating to local field-aligned coordinates ($x_{\parallel}, x_{\perp 1}, x_{\perp 2}$), and we linearly interpolate the DES sky maps in time and azimuth to ensure the same portion of velocity space is being compared between spacecraft. This computation of ∇f_e assumes that the linear, four-spacecraft gradient is a valid approximation of the true gradient, which requires that the spatial gradient length scale be sufficiently large compared to the inter-spacecraft separations. Typically, this assessment is performed by comparing the characteristic length scale of the system to the local thermal gyroradius, $r_{th} = m v_{th} / e B$. Although this approach is valid in an average sense, the ∇f_e measurements are computed throughout velocity space, so that the relevant spatial scale may be considered in a velocity-dependent fashion: $r(v) = m v / e B$. Consequently, for events with an average gradient length scale that is comparable to the spacecraft separation, the finite difference estimation of ∇f_e may be less accurate for lower-energy electrons with $v < v_{th}$ (which have gyroradii that may be smaller than the average spacecraft separation), whereas ∇f_e will become more accurate for higher-energy electrons with $v > v_{th}$. We also note an application of drift-kinetic theory reported recently as an alternate way of computing gradients of plasma properties from observed non-gyrotropic features of the distribution function⁵⁹.

Maxwellian model for ∇f_e . The ∇f_e model is derived from the drifting Maxwellian distribution given by

$$f_e = n_e \left(\frac{m_e}{2\pi T_e} \right)^{3/2} \exp \left[-\frac{m_e}{2T_e} \left(v_{\parallel}^2 + (v_{\perp 1} - U_{e\perp 1})^2 + v_{\perp 2}^2 \right) \right] \quad (10)$$

We allow the plasma to drift in the $v_{\perp 1}$ direction with an electron bulk velocity $U_{e\perp 1}$ arising mainly from the $E \times B$ drift ($U_{E \times B}$) and diamagnetic drift ($U_{*,e}$) terms: $U_{e\perp 1} \approx U_{E \times B} + U_{*,e} = \left(\mathbf{E} + \frac{\nabla \cdot \mathbf{P}_e}{en_e} \right) \times \mathbf{B} / B^2$. With this velocity $U_{e\perp 1}$, equation (10) is an approximate solution to the Vlasov equation for events when the gradient length scale is larger than the spacecraft separation⁶⁰. Although it is well known that a drifting Maxwellian distribution cannot, in general, provide an exact solution to the Vlasov equation for the more complicated cases of bulk velocity or temperature gradients considered in this Article, useful insight may nevertheless be obtained from this model for ∇f_e , as discussed in the main text. Dividing equation (1) by f_e , the normalized Maxwellian gradient distribution $\nabla f_e / f_e$ exhibits a quadratic dependence on the velocity-space coordinates:

$$\frac{\nabla f_e}{f_e} = \mathbf{a} v^2 + \mathbf{b} v' + \mathbf{c} \quad (11)$$

$$\mathbf{a} = \left(\frac{1}{v_{th}^2} \right) \frac{\nabla T_e}{T_e}, \quad \mathbf{b} = \left(\frac{2}{v_{th}^2} \right) \nabla U_{e\perp 1}, \quad \mathbf{c} = \frac{\nabla n_e}{n_e} - \frac{3}{2} \frac{\nabla T_e}{T_e} \quad (12)$$

where we let $v' = v_{\perp 1} - U_{e\perp 1}$ and $v^2 = (v_{\parallel}^2 + v'^2 + v_{\perp 2}^2)$ to highlight the quadratic form of equation (11).

Focusing on the $\perp_1\text{--}\perp_2$ dependence of ∇f_e , we consider only velocity-space slices of ∇f_e in the perpendicular $v_{\perp 1}\text{--}v_{\perp 2}$ plane centred at the parallel bulk velocity ($v_{\parallel} = U_{e\parallel}$). Thus, for simplicity, $U_{e\parallel}$ has been neglected in equation (10) because $(v_{\parallel} - U_{e\parallel}) = 0$ for the slices considered, although in general the spatial variation of $U_{e\parallel}$ would become important when considering arbitrarily oriented ∇f_e slices. For completeness, here we note that for a model Maxwellian shifted by a general bulk velocity $U_e(\mathbf{x})$, the gradient equation (1) would have the following form:

$$\nabla f_e = \left[\frac{\nabla n_e}{n_e} + \left(\frac{2(\mathbf{v} - \mathbf{U}_e) \cdot \nabla \mathbf{U}_e}{v_{th}^2} \right) + \left(\frac{(\mathbf{v} - \mathbf{U}_e)^2}{v_{th}^2} - \frac{3}{2} \right) \frac{\nabla T_e}{T_e} \right] f_e \quad (13)$$

The model ∇f_e and $\mathbf{v} \cdot \nabla f_e$ structures in Fig. 1 are best understood by considering two Maxwellians, f_1 and f_2 , spatially separated by an amount $\Delta x = x_2 - x_1$ along the \perp_2 direction. Provided that Δx is sufficiently small compared to the scale length of the gradient, then $\nabla_{\perp 2} f_e \approx (f_2 - f_1) / \Delta x$ is a valid approximation. Figure 1a–d corresponds to the case when $(\nabla n_e)_{\perp 2} > 0$, with both $\nabla U_{e\perp 1}$ and ∇T_e equal to 0. The solid and dashed lines in Fig. 1b represent f_1 and f_2 , respectively. The red arrow pointing from f_1 to f_2 in Fig. 1b indicates the positive increase in phase-space density experienced when moving into the density gradient (going from x_1 to x_2). Multiplication of $\nabla_{\perp 2} f_e$ by $v_{\perp 2}$ results in the bipolar structure of $v_{\perp 2} \nabla_{\perp 2} f_e$ along $v_{\perp 2}$ (Fig. 1c,d). Figure 1e–h corresponds to $(\nabla U_{e\perp 1})_{\perp 2} < 0$, which is chosen to compare with the MMS observations discussed in the main text. For this case, the bulk velocity gradient $(\nabla U_{e\perp 1})_{\perp 2} < 0$ requires that f_2 be shifted to the left of f_1 so that $\nabla_{\perp 2} f_e$ acquires a bipolar structure along the $v_{\perp 1}$ direction (Fig. 1f). Consequently, multiplication by $v_{\perp 2}$ results in a symmetric, quadrupolar velocity-space structure in $v_{\perp 2} \nabla_{\perp 2} f_e$ (Fig. 1g). In Fig. 1i–l, the temperature gradient $(\nabla T_e)_{\perp 2} > 0$ results in a ring structure in the 2D slice (Fig. 1i), a tripolar 1D cut of $\nabla_{\perp 2} f_e$ (Fig. 1j) and a quadrupolar structure $v_{\perp 2} \nabla_{\perp 2} f_e$ along $v_{\perp 2}$ (Fig. 1k,l). These $\nabla_{\perp 2} f_e$ structures associated with ∇T_e are due to the Maxwellian's temperature dependence, which is discussed in the main text. For the situation shown in Fig. 1m–p, each of the gradients ∇n_e , $\nabla U_{e\perp 1}$ and ∇T_e contributes to the resulting structure of $\nabla_{\perp 2} f_e$ and $v_{\perp 2} \nabla_{\perp 2} f_e$. The result is a bipolar crescent structure in $\nabla_{\perp 2} f_e$ (Fig. 1m) and an asymmetric, skewed quadrupole structure in $v_{\perp 2} \nabla_{\perp 2} f_e$ (Fig. 1o). This more complicated visual structure is produced mainly from the $(\nabla U_{e\perp 1})_{\perp 2} > 0$ and $(\nabla \cdot \mathbf{T}_e)_{\perp 2} > 0$ gradients, which operate together to generate the shifted ring and asymmetric quadrupole features.

MMS event selection. The ideal choice of events for this study comprises those that isolate the effects of the electron density ∇n_e , bulk velocity ∇U_e and temperature ∇T_e gradients, so the corresponding ∇f_e structures may be considered independently for each case. We focus on events for which the gradient is mostly aligned with the \perp_2 direction. This is a common gradient orientation for electron-scale currents whenever the electrons decouple from the bulk ion motion and move at roughly the $E \times B$ velocity, which results in the current density \mathbf{J} directed along the negative \perp_1 direction. Consequently, from the force balance, $\mathbf{J} \times \mathbf{B} = \nabla \cdot \mathbf{P}$, the gradient direction points roughly along the $(-\perp_1) \times (\hat{\mathbf{J}}) = \hat{\perp}_2$ direction^{50,61}. Because the gradients sustaining the current layers reported here were predominantly directed along the \perp_2 direction, our focus on the \perp_2 component of the gradient distribution $\nabla_{\perp 2} f_e$ and corresponding approximation $\mathbf{v} \cdot \nabla f_e \approx v_{\perp 2} \nabla_{\perp 2} f_e$ accounts for the majority of the kinetic, velocity-space structures observed by MMS. For more complicated current layers with inherently 2D or 3D pressure gradient structures oriented along more than just one of the field-aligned coordinate directions, the other gradient distributions $\nabla_{\perp 1} f_e$ and $\nabla_{\parallel} f_e$ would become important.

Suitable intervals where the ∇n_e and ∇T_e effects can be studied separately are selected from a reported magnetopause reconnection event exhibiting filamentary electron currents on 22 October 2015 around 6:05 UT (ref. 52). The thin current sheet encountered by MMS on 1 October 2016 near 18:19:24 UT serves as a prime example of the effect of ∇U_e , and is particularly useful for resolving spatial gradients because of the remarkably close spacecraft separation at this time, which was less than 5 km for MMS 2 and MMS 3 (the average spacecraft separation was ~ 6.4 km). In addition, we consider one of the recently analysed thin electron-scale current sheets with a thickness on the order of a few electron skin depths⁵⁰ as an example of how a combination of ∇n_e , ∇U_e and ∇T_e gradients influences the structure of ∇f_e . The gradient length scale for all of the events in this study is on the order of 1 to 10 thermal electron gyroradii, and the peak electron bulk velocity ranges from 25% to 30% of the local electron thermal velocity for the three events exhibiting ∇U_e or ∇T_e gradients.

For these magnetopause events, the relevant electron velocities are on the order of several times the thermal speed: $v \approx 10,000 \text{ km s}^{-1}$. Thus, the average electron is travelling so fast through the local spatial gradients that explicit time variations of the velocity distribution would not be able to contribute significantly to the electron dynamics. For example, if we compare a particular variation of Δf_e detected in a time interval $\Delta t = 30 \text{ ms}$ to an equivalent Δf_e variation measured between spacecraft separated by $\Delta x \approx 10 \text{ km}$ for a thermal electron, we find

$$\frac{|\partial f_e / \partial t|}{|\mathbf{v} \cdot \nabla f_e|} \approx \frac{(\Delta f_e / \Delta t)}{v_{th} (\Delta f_e / \Delta x)} = \frac{(\Delta x / \Delta t)}{v_{th}} \approx \frac{(10 \text{ km}) / (0.03 \text{ s})}{(10,000 \text{ km s}^{-1})} \approx 0.033 \quad (14)$$

Similarly, for an $(\mathbf{F}/m_e) \cdot \nabla f_e$ measurement taken between adjacent velocity-space bins with $\Delta v \approx 1,000 \text{ km s}^{-1}$ (which is the velocity separation of the DES energy targets near 200 eV, the energy roughly corresponding to the thermal velocity) and a typical force due to an electric field on the order of $E \approx 10 \text{ mV m}^{-1}$, we have

$$\frac{|\partial f_e / \partial t|}{|(\mathbf{F}/m_e) \cdot \nabla f_e|} \approx \frac{(\Delta f_e / \Delta t)}{(eE/m_e)(\Delta f_e / \Delta v)} = \frac{(\Delta v / \Delta t)}{(eE/m_e)} \approx \frac{(1,000 \text{ km s}^{-1}) / (0.03 \text{ s})}{(1.8 \times 10^6 \text{ km s}^{-2})} \approx 0.019 \quad (15)$$

If we had used $|\mathbf{F}| \approx e(v_{th} B)$ instead of $eE \approx eU_e B$ (where $U_e \approx 1,000 \text{ km s}^{-1}$), then the ratio in equation (15) would be almost another order of magnitude smaller. Thus, explicit time variations in $\partial f_e / \partial t$ taking place during a 30-ms interval can be reasonably neglected compared to the spatial and velocity-space variations observed by MMS throughout most of velocity space. In this steady-state limit ($\partial f_e / \partial t = 0$), the Vlasov equation in field-aligned coordinates becomes

$$v_{\perp 2} \nabla_{\perp 2} f_e - \frac{eE_{\perp 2}}{m_e} \frac{\partial f_e}{\partial v_{\perp 2}} - \frac{eB}{m_e} \left(v_{\perp 2} \frac{\partial f_e}{\partial v_{\perp 1}} - v_{\perp 1} \frac{\partial f_e}{\partial v_{\perp 2}} \right) = 0 \quad (16)$$

Here, we assume that E_{\parallel} is sufficiently small compared to E_{\perp} so that the term $E_{\parallel} \partial f_e / \partial v_{\parallel}$ can be neglected. Additionally, $E_{\perp 1} \approx 0$ in these field-aligned coordinates, because the \perp_1 direction is roughly along the $\mathbf{E} \times \mathbf{B}$ direction (perpendicular to \mathbf{E}).

Data availability

All MMS data are available to the public via <https://lasp.colorado.edu/mms/sdc/public/>.

Code availability

The code used to plot the MMS gradient distributions will be made available upon reasonable request.

References

57. Gurnett, D. A. & Bhattacharjee, A. *Introduction to Plasma Physics: With Space and Laboratory Applications* (Cambridge Univ. Press, 2005).
58. Harvey, C. C. in *Analysis Methods for Multi-Spacecraft Data* ISSI Scientific Reports Series (eds Paschmann, G. & Daly, P. W.) 307–322 (ISSI/ESA, 1998).
59. Wetherton, B. A., Egedal, J., Montag, P., Le, A. & Daughton, W. A drift-kinetic method for obtaining gradients in plasma properties from single-point distribution function data. *J. Geophys. Res. Space Phys.* **125**, e2020JA027965 (2020).
60. Hazeltine, R. D. & Meiss, J. D. *Plasma Confinement* (Addison-Wesley, 1992).

61. Graham, D. B. et al. Electron currents and heating in the ion diffusion region of asymmetric reconnection. *Geophys. Res. Lett.* **43**, 4691–4700 (2016).

Acknowledgements

We especially thank the MMS instrument teams for their dedication and commitment to providing unprecedented, high-quality datasets. J.R.S. thanks L. Morrison for helpful discussions regarding the intricacies of phase space. This research was supported in part by NASA grants to the Fast Plasma Investigation, FIELDS team and Theory and Modeling programme of the MMS mission. J.R.S. was supported by NASA grants 80NSSC19K1092 and 80NSSC21K0732. S.W. was supported by NASA grant 80NSSC18K1369 and DOE grant DE-SC0020058. P.A.C. was supported by NASA grants NNX16AG76G and 80NSSC19M0146, NSF grants AGS-1602769 and PHY-1804428 and DOE grant DE-SC0020294. R.E.D. was supported by NASA grant 80NSSC19K0254. V.M.U. was supported by NASA grant NNG11PL10A.

Author contributions

J.R.S. performed the MMS multi-spacecraft data analysis, developed the analytical model for comparison to the MMS observations and prepared the manuscript. D.J.G. and J.C.D. assisted with interpretation of the plasma distribution and gradient structures, the use of MMS FPI data, and the preparation of the text and figures. B.L.G. supported the project at both the institutional and mission levels, and helped to ensure the overall quality of the MMS and FPI data. S.W., N.B. and L.-J.C. aided in the interpretation of the kinetic velocity distribution measurements in the context of magnetopause magnetic reconnection observations. P.A.C., S.J.S., R.E.D. and C.S. offered careful critiques of the scientific results, figures and conclusions of the manuscript, and provided useful feedback regarding contextual and relevant literature related to this research. V.M.U. and W.R.P. provided insightful feedback and discussion regarding the data-model comparisons and concerning the overall conclusions and future implications of this research. A.F.V., J.N. and L.A.A. assisted with the overall interpretation of the results. D.E.d.S. offered technical support and data analysis tools that aided in the identification of the MMS events presented in the manuscript. R.B.T. assisted with the interpretation of the electric-field data in comparison to the particle measurements.

Competing interests

The authors declare no competing interests.

Additional information

Correspondence and requests for materials should be addressed to J.R.S.

Peer review information *Nature Physics* thanks Jan Egedal and the other, anonymous, reviewer(s) for their contribution to the peer review of this work.

Reprints and permissions information is available at www.nature.com/reprints.